Climatology, Seasonality, and Trends of Spatially Coherent Ocean Eddies

Josué Martínez-Moreno, Andrew Mcc. Hogg, Matthew H. England

▶ **To cite this version:**

Josué Martínez-Moreno, Andrew Mcc. Hogg, Matthew H. England. Climatology, Seasonality, and Trends of Spatially Coherent Ocean Eddies. Journal of Geophysical Research. Oceans, 2022, 127, 10.1029/2021JC017453 . insu-03779394

HAL Id: insu-03779394

https://insu.hal.science/insu-03779394

Submitted on 16 Sep 2022

HAL is a multi-disciplinary open access archive for the deposit and dissemination of scientific research documents, whether they are published or not. The documents may come from teaching and research institutions in France or abroad, or from public or private research centers.

L'archive ouverte pluridisciplinaire **HAL**, est destinée au dépôt et à la diffusion de documents scientifiques de niveau recherche, publiés ou non, émanant des établissements d'enseignement et de recherche français ou étrangers, des laboratoires publics ou privés.

Distributed under a Creative Commons Attribution 4.0 International License

Check for updates

JGR Oceans

RESEARCH ARTICLE
10.1029/2021JC017453

Climatology, Seasonality, and Trends of Spatially Coherent Ocean Eddies

Josué Martínez-Moreno[1,2], Andrew McC. Hogg[1], and Matthew H. England[3]

[1]Research School of Earth Science and ARC Center of Excellence for Climate Extremes, Australian National University, Canberra, ACT, Australia, [2]Now at Laboratoire d'Océanographie Physique et Spatiale (LOPS), University of Brest/IFREMER/IRD/CNRS, Brest, France, [3]Climate Change Research Centre (CCRC), UNSW Australia, Sydney, NSW, Australia

Key Points:

- Coherent eddies contain around half of the total surface ocean eddy kinetic energy
- The seasonal cycle of the abundance and amplitude of spatially coherent eddies reveals a 3–6 months lag to wind forcing
- The seasonal lag between the number and the amplitude of spatially coherent eddies suggests a role for the inverse energy cascade

Correspondence to:
J. Martínez-Moreno,
josue.martinez.moreno@ifremer.fr

Citation:
Martínez-Moreno, J., Hogg, A. M., & England, M. H. (2022). Climatology, seasonality, and trends of spatially coherent ocean eddies. *Journal of Geophysical Research: Oceans*, *127*, e2021JC017453. https://doi.org/10.1029/2021JC017453

Received 21 APR 2021
Accepted 28 JUN 2022

Author Contributions:
Conceptualization: Josué Martínez-Moreno, Andrew McC. Hogg, Matthew H. England
Data curation: Josué Martínez-Moreno
Formal analysis: Josué Martínez-Moreno
Investigation: Josué Martínez-Moreno, Andrew McC. Hogg, Matthew H. England
Methodology: Josué Martínez-Moreno
Resources: Andrew McC. Hogg
Software: Josué Martínez-Moreno
Supervision: Andrew McC. Hogg, Matthew H. England
Writing – original draft: Josué Martínez-Moreno
Writing – review & editing: Josué Martínez-Moreno, Andrew McC. Hogg, Matthew H. England

© 2022. The Authors.
This is an open access article under the terms of the Creative Commons Attribution License, which permits use, distribution and reproduction in any medium, provided the original work is properly cited.

Abstract Ocean eddies influence regional and global climate by mixing and transporting heat, carbon, nutrients, and other properties. One of the most recognizable and ubiquitous features of oceanic variability are mesoscale eddies (vortices and meanders/jets) with spatial scales of tens to hundreds of kilometers. Vortices resemble Gaussian-like features in sea surface height which locally affect near-surface wind, cloud properties, and rainfall patterns; we refer to these Gaussian-like eddies as spatially coherent eddies. Although spatially coherent eddies are ubiquitous, their climatology, seasonality, and long-term temporal evolution is yet to be explored. Here, we examine the kinetic energy (KE) contained in spatially coherent eddies and present their temporal variability using satellite observations between 1993 and 2020. Around half of the transient KE contained by eddies corresponds to spatially coherent eddies. A strong seasonal cycle is observed in the spatially coherent eddy field, and correlates with the wind forcing at time-lags of 3–6 months. The seasonal correlation between wind forcing and spatially coherent eddies with diameters smaller than 120 km is faster (~3 months), than that of coherent eddies with larger diameters (~6 months). These lags between different spatially coherent eddy scales are consistent with the transfer of energy from small to large scales (inverse energy cascade). Our analysis highlights the relative importance of the spatially coherent eddy field in the KE budget, revealing a lagged response between the spatially coherent eddy and forcing at different time-scales, and showcases the seasonality, and multidecadal trends of coherent eddy properties over the global ocean.

Plain Language Summary Spatially coherent vortices are a ubiquitous feature of ocean variability observable from satellites. These eddies are crucial in ocean dynamics as they interact with the atmosphere and some can transport properties over long distances. Our study investigates the seasonal, interannual, and long-term changes in the number and intensity of spatially coherent vortices, by automatically identifying individual vortices over the available satellite altimeter record. The seasonal cycle suggests a transition from numerous, smaller, and weaker spatially coherent vortices, to fewer, larger, and stronger spatially coherent vortices over the season. In addition, a long-term adjustment of the spatially coherent field is identified with possible links to long-term changes in the climate system.

1. Introduction

Mesoscale ocean variability with spatial scales of tens to hundreds of kilometers is comprised of features such as vortices, waves, and jets (Ferrari & Wunsch, 2009; Fu et al., 2010). These mesoscale processes are highly energetic, and they play a crucial role in the transport of heat, salt, momentum, and other tracers through the ocean (Danabasoglu et al., 1994; Dufour et al., 2015; Gill et al., 1974; Wunsch & Ferrari, 2004; Wyrtki et al., 1976). The central focus of this study are mesoscale spatially coherent eddies defined as oceanic vortices with spatial scales ranging from approximately 10 to 100 km that induce a Gaussian signature in the sea surface height anomaly (SSHa). Spatially coherent eddies are one of the most recognizable and abundant ocean features observable from satellite observations; a subset, the non-linear coherent eddies are capable to transport water properties, which makes them essential to the dynamics of oceans as concluded by many previous studies (Beron-Vera et al., 2013; Frenger et al., 2013, 2015; Hogg & Blundell, 2006; Patel et al., 2020; Pilo et al., 2015; Schubert et al., 2019; Siegel et al., 2011). An important distinction must be made to differentiate the usage of the terms "spatially coherent eddies" and "coherent eddies" in previous literature. The first, "spatially coherent eddies" refer to the spatial Gaussian signature of mesoscale vortices in the SSHa field, independent of their lifespan. Two subsets of the spatially coherent eddies, time-tracked eddies and non-linear eddies have been referred in literature as "coherent eddies" due to their capability to transport properties across vast distances in the ocean (Beron-Vera

et al., 2013; Chelton et al., 2011). Hereafter, for simplicity we interchangeably use the terms "spatially coherent" and "coherent" to refer to mesoscale vortices with a Gaussian imprint on the SSHa field; when referring to the canonical usage of "coherent eddies" first described by Chelton et al. (2011), we will use "time-tracked eddies."

Spatially coherent eddies are quasi-circular geostrophic currents. According to their rotational direction and the sign of the Coriolis parameter, the SSHa within a coherent eddy resembles either a negative or a positive Gaussian. This characteristic SSHa signature of spatially coherent eddies has been utilized to identify and track eddies from satellite altimetry (e.g., Ashkezari et al., 2016; Chelton et al., 2007; Cui et al., 2020; Faghmous et al., 2015; Martínez-Moreno et al., 2019). Automated algorithms for identification of coherent eddies have revealed their ubiquity in the oceans and their strong influence at hotspots of eddy activity such as in boundary current extensions and the Antarctic Circumpolar Current. In these hotspots, it has been estimated that time-tracked eddies with lifespans greater than 4 weeks contribute at least 40%–50% of the net mesoscale kinetic energy (KE) (Chelton et al., 2011) and thus a significant fraction of the total KE (Ferrari & Wunsch, 2009). Although this estimate showcases the importance of the time-tracked eddy field, the energy contained in time-tracked eddies as reported by Chelton et al. (2011) was estimated by extracting the total geostrophic velocity within a circle of radius encompassing each detected coherent eddy; thus, this estimate not only contains energy from time-tracked eddies, but also other processes (meanders). Thus, here we extend on this past work by reconstructing the surface imprint of all features resembling a Gaussian in the sea surface height (SSH) (spatially coherent eddies) using the eddy-tracking algorithm of Martínez-Moreno et al. (2019) and the available satellite record until June 2020.

There is broad consensus that mesoscale eddy kinetic energy (EKE) has a pronounced seasonal variability (Kang & Curchitser, 2017; Qiu, 1999; Qiu & Chen, 2004; Uchida et al., 2017). Several hypotheses have been proposed to explain this seasonality including: seasonal variations of atmospheric forcing (Sasaki et al., 2014), seasonality of the mixed layer depth (Callies et al., 2015; Qiu et al., 2014), seasonality of the intensity of barotropic instability (Qiu & Chen, 2004), the variability of the baroclinic instability due to the seasonality of the vertical shear (Qiu, 1999), and a seasonal lag of the inverse energy cascade (i.e., energy is transferred between scales, from small to large; Arbic et al., 2013) in combination with the presence of a front in the mixed layer, which can lead to a seasonal cycle of the baroclinic instability (Qiu et al., 2014). On one hand, processes such as barotropic and baroclinic instabilities control the seasonality of mesoscale eddies in the ocean. On the other hand, recent studies using observations and eddy-permitting climate models show a multidecadal increase in the ocean stratification (Li et al., 2020), a horizontal readjustment of sea surface temperature gradients (Bouali et al., 2017; Cane et al., 1997; Ruela et al., 2020), and an intensification of the KE, the EKE, and the mesoscale EKE over the last 3 decades (Hu et al., 2020; Martínez-Moreno et al., 2021; Wunsch, 2020). All these seasonal and long-term adjustments control the response of the mesoscale eddy field and by inference they also influence the seasonality and trends of the spatially coherent eddies, a component of the mesoscale field. However, due to the limited temporal and spatial resolution of ocean observations, exploring the exact effect of these mechanisms is beyond the scope of this study, where we instead focus on quantifying the seasonality and long-term trends of the spatially coherent component of the eddy field.

Here we present the data sources and method used in Martínez-Moreno et al. (2019) to extend the spatial coverage from the Southern Ocean to a global climatology of spatially coherent eddies and their properties (number, intensity, and diameter), including abundance and intensity (Section 2). Then, in Section 3.1, we estimate the KE contained by coherent vortices and non-coherent features (e.g., jets and meanders), and the global seasonality of coherent EKE. In Sections 3.2–3.4, we provide an estimate of the EKE contained in coherent eddies, the seasonal cycle of the coherent EKE, and the seasonal cycle and long-term trends of the coherent eddy properties over the satellite record. In Section 3.5, we focus our attention on the seasonal cycle of coherent eddy properties in regions dominated by coherent eddies. Finally, Section 4 summarizes the main results and discusses the implications of this study. To our knowledge, this is the first climatological and seasonality study focusing on the spatially coherent eddy component of the mesoscale eddy field.

2. Methods

We use the all-satellite SSH data made available by the Copernicus Marine Environment Monitoring Service (CMEMS, 2017). This gridded product contains daily SSH and geostrophic velocities with a 0.25° spatial resolution between January 1993 and June 2020. The daily geostrophic velocities allow us to compute the KE and EKE

over the satellite record. The primary source of energy in the ocean surface is exerted by wind stress (Ferrari & Wunsch, 2009); therefore, we compare the seasonal cycle of the spatially coherent eddies and the seasonal cycle of the wind magnitude from the JRA55 reanalysis (Japan Meteorological Agency, Japan, 2013) using wind velocities at 10m above the ocean's surface.

Over the same period (1993–2020), we use the method presented by Martínez-Moreno et al. (2019), hereafter MM19, to reconstruct the KE contained by spatially coherent eddy processes (coherent eddy kinetic energy; CEKE). This method defines geometrically spatially coherent eddies as two-dimensional Gaussian features, and it is able to estimate the surface signature of individual eddies using an optimally fitted Gaussian. Aggregates of the Gaussian surface fitted to each individual eddy allow us to estimate the KE of the spatially coherent eddy field using the geostrophic approximation. As such, the EKE field can be decomposed into: coherent eddies (vortices) and non-coherent features (such as jets and meanders). The method of MM19 provides coherent eddy statistics such as their abundance, amplitude, and diameter. Using this approach we do not track individual eddies over time, and therefore no minimum lifetime criterion is used to filter the coherent eddy statistics.

Climatological quantities of the spatially coherent eddy properties are qualitatively compared with the time-tracked eddy data set released by Chelton and Schlax (2013), hereafter CS13. MM19 and CS13 automatically identify individual eddies using closed contours from the 0.25° SSH anomaly data set after spatial filters are applied to remove large-scale features. To compare spatially coherent and time-tracked eddy statistics between datasets, the individually identified eddy properties in both datasets are first re-gridded to a 1° resolution grid. The qualitative comparisons presented in this study are used to validate that both methods resolve the spatial patterns of coherent eddies. However, it is important to note that these datasets differ in the criteria used to identify and record eddy statistics. The major differences include: (a) MM19's algorithm requires a good fit between a 2D Gaussian and the SSH anomaly (SSHa) surface within the identified closed contour, while CS13's only uses the outermost closed contour of SSH; (b) MM19's data set reports the maximum absolute SSHa within the identified spatially coherent eddy, while CS13's algorithm reports the maximum SSH value minus the discrete level in which the time-tracked eddy was identified; and (c) the definition of spatially coherent eddies used in this study relates to the geometrical signature of quasi-circular currents, rather than a lifespan threshold, thus MM19's data set includes all coherent eddies for which the individual 2D Gaussian fit of each coherent eddy candidate has a skill larger than 90%, while CS13's data set excludes mesoscale eddies candidates when their lifetimes are shorter than 4 weeks and their amplitude smaller than 1 cm. The time-filtering applied in CS13's data set after time-tracking eddies, makes CS13's data set a subset of the spatially coherent eddies identified in MM19. This inference is possible due to the strong smoothing applied on the processing satellite observations processing (Amores et al., 2018), as well as evidence of time-tracked eddies being quasi-circular vortices on composites of SSH and velocities (Chelton et al., 2011; Faghmous et al., 2015).

2.1. Kinetic Energy Decomposition

Kinetic energy is commonly decomposed with a Reynolds decomposition of the surface velocity field, $\mathbf{u} = (u, v)$ where the velocity field is split into the time-mean $(\overline{\mathbf{u}})$ and time-varying components $(\mathbf{u}')$. Moreover, MM19 proposed to further decompose the time-varying component into spatially coherent features $(\mathbf{u}'_\mathbf{e})$ and non-coherent features $(\mathbf{u}'_\mathbf{n})$. Therefore the KE decomposes as follows:

$$\mathrm{KE} = \underbrace{\overline{u}^2 + \overline{v}^2}_{\mathrm{MKE}} + \underbrace{\underbrace{u'^2_e + v'^2_e}_{\mathrm{CEKE}} + \underbrace{u'^2_n + v'^2_n}_{\text{non-CEKE}} + \mathcal{O}_c}_{\mathrm{EKE}} + \mathcal{O}. \tag{1}$$

Due to the properties of this decomposition, the term $\mathcal{O} = \overline{u}u' + \overline{v}v'$ is zero by definition when averaged over the same period as $\overline{\mathbf{u}}$. However, $\mathcal{O}_c = u_e u_n + v_e v_n$ is not necessarily negligible, unless it is averaged over time and space. More information about the decomposition of the field into coherent features and non-coherent features is explained in Martínez-Moreno et al. (2019). A global snapshot of each component of KE decomposition is shown in Figure 1. The KE and EKE are dominated by rings and filaments. As expected, the decomposition into CEKE exhibits only the ring-like signatures expected of spatially coherent eddies (vortices; Figure 1f), while non-CEKE, the non-coherent component, primarily shows filaments (e.g., jets and meanders; Figure 1h), with some misidentified coherent eddies.

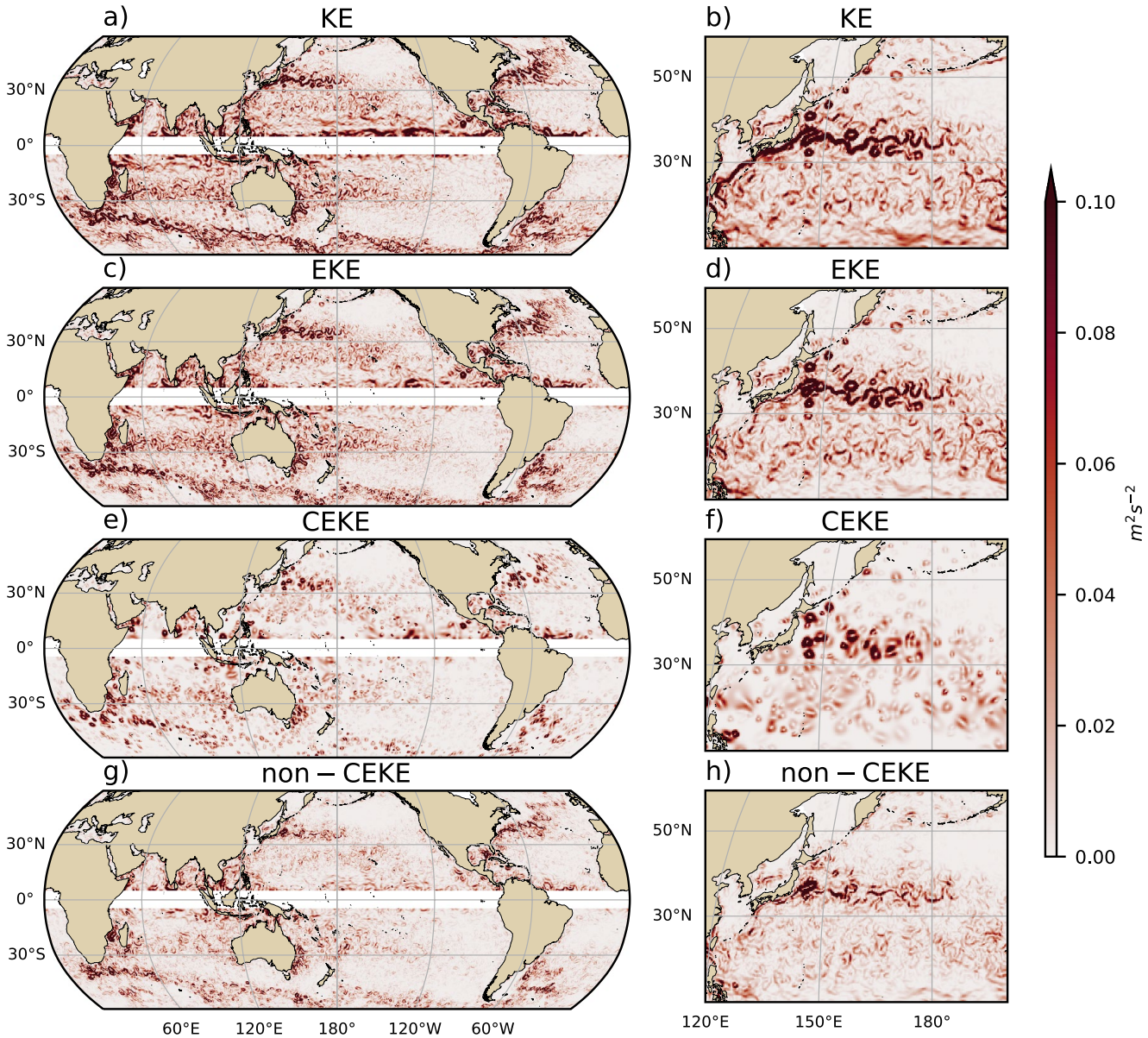

Figure 1. Snapshot of global and Kuroshio Current surface kinetic energy (KE; a, b), surface eddy kinetic energy (EKE; c, d), surface spatially coherent eddy kinetic energy (CEKE; e, f), and surface non-coherent eddy kinetic energy (non-CEKE; g, h) for the first of January 2017.

2.2. Eddy Statistics

The eddy statistics used in this study include (a) the eddy count (cEddy_n) defined as the number of spatially coherent eddies, (b) the eddy diameter (cEddy_d) defined as the diameter of a circle with equal area to the closed contour of each identified eddy, and (c) positive definite $\left(\text{cEddy}^+_{amp}\right)$ and negative definite $\left(\text{cEddy}^-_{amp}\right)$ coherent eddy amplitudes, defined as the mean amplitude of positive and negative SSHa, respectively. The mean eddy amplitude ($\text{cEddy}_{\text{amp}}$) is defined as the average amplitude of positive and negative coherent eddies, thus it can be negative or positive where a given polarity of coherent eddies dominate a region. To remove this polarity dependence, we also compute the polarity independent eddy amplitude ($\text{cEddy}_{|\text{ampl}|}$) defined as:

$$\text{cEddy}_{|amp|} = \frac{1}{2}\left(\text{cEddy}^+_{amp} - \text{cEddy}^-_{amp}\right). \quad (2)$$

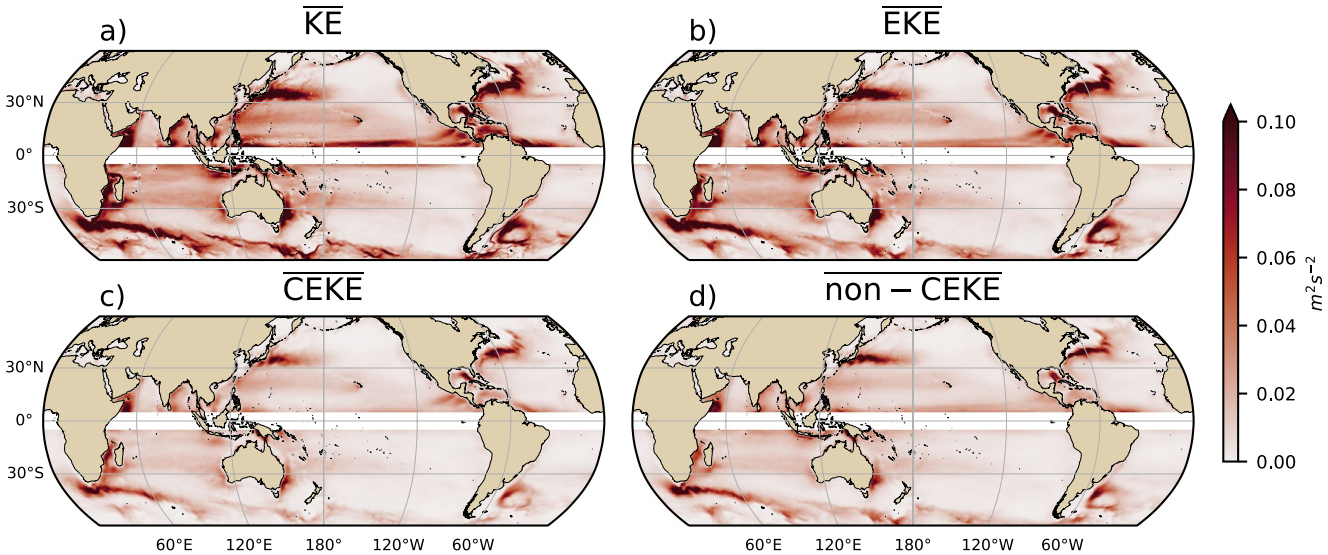

Figure 2. (a) Mean surface kinetic energy ($\overline{KE}$); (b) surface eddy kinetic energy ($\overline{EKE}$); (c) surface spatially coherent eddy kinetic energy ($\overline{CEKE}$), and (d) surface non-coherent eddy kinetic energy ($\overline{non\text{-}CEKE}$) averaged between 1993 and 2018.

We analyze the climatology and trends of the above eddy statistics over the available satellite record, namely between 1993 and 2020. We exclude the equatorial region (10°S–10°N) and regions poleward of 60°, because the geostrophic approximation is invalid near the Equator and the satellite spatial coverage at high-latitudes is unable to resolve the coherent eddy scales polewards of 60°. Note that the climatology of $cEddy_n$ is computed by adding all the identified eddies over the record, while all other climatological statistics are computed as the time-average over the record. Seasonal climatologies are calculated for the monthly average of each coherent eddy statistic, while hemispheric time-series are filtered with a running average of 90 days. Trends of $cEddy_n$ and $|cEddy_{amp}|$ are calculated by coarsening the data set to a 5° grid, and then linear trends are computed for each grid point. The statistical significance of trends is assessed by a modified Mann-Kendall test above the 95% confidence level (Yue & Wang, 2004).

Time averages are denoted by $\bar{}$, while area-weighted averages are denoted using $\langle\,\rangle$, where the area-weighted average of a function f is:

$$\langle f \rangle = \frac{\int f \xi dx dy}{\int \xi dx dy}, \tag{3}$$

where ξ is a mask set to zero in areas where no coherent eddies are identified and one elsewhere. This mask is only applied to spatial averages of the eddy amplitude to avoid averaging with zero values where no eddies were identified. No other field uses this mask.

3. Results

3.1. Global Spatially Coherent Eddy Energetics

The KE decomposition estimated from SSH measured by satellite altimeters averaged from 1993 to 2020 is shown in Figure 2. These maps show that many regions of the ocean are highly energetic in mean total KE ($\overline{KE}$), mean EKE ($\overline{EKE}$), mean spatially CEKE ($\overline{CEKE}$) and mean non-coherent eddy kinetic energy (non-CEKE) ($\overline{non\text{-}CEKE}$). The spatial pattern highlights well-known regions of the ocean where mesoscale processes are abundant, such as the western boundary current (WBC) extensions and the Antarctic Circumpolar Current. The spatial distribution of the energy contained by the reconstructed mesoscale coherent eddies and non-coherent components are of similar magnitude (Figures 2c and 2d). However, there are some regions where coherent eddies dominate over non-coherent, and vice-versa. Overall, this decomposition suggests that boundary current

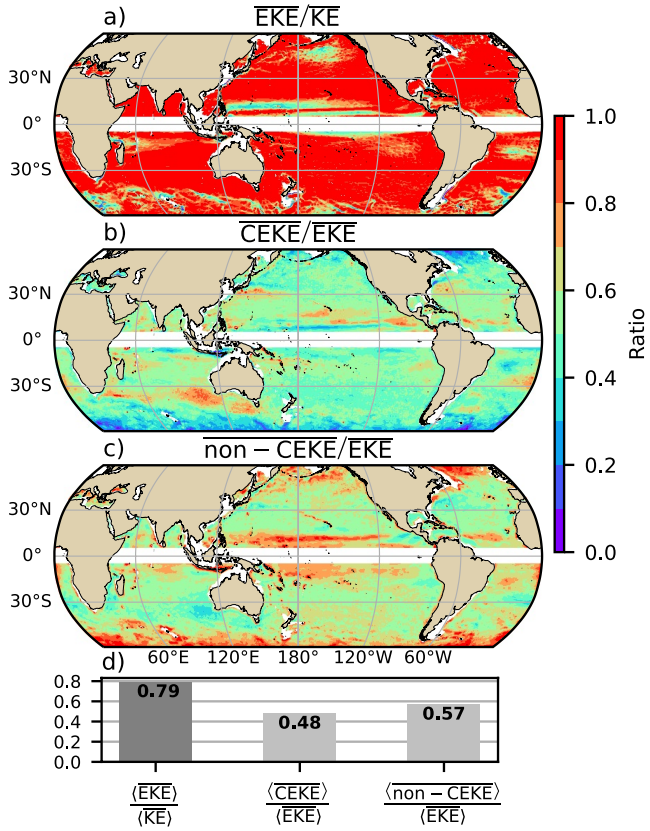

Figure 3. Ratios of the kinetic energy components. (a) Map of the proportion of mean eddy kinetic energy ($\overline{EKE}$) vs. mean total kinetic energy ($\overline{KE}$); (b) Map of the fraction of mean spatially coherent eddy kinetic energy ($\overline{CEKE}$) vs. mean eddy kinetic energy ($\overline{EKE}$); (c) Map of the fraction of mean non-coherent eddy kinetic energy (non-$\overline{CEKE}$) vs. mean eddy kinetic energy ($\overline{EKE}$); (d) Global time and area averaged (represented by $\langle\ \rangle$) fraction of mean eddy kinetic energy ($\langle\overline{EKE}\rangle$) versus the global mean kinetic energy ($\langle\overline{KE}\rangle$), area averaged fraction of mean coherent eddy kinetic energy ($\langle\overline{CEKE}\rangle$) and mean non-coherent eddy kinetic energy ($\langle$non-$\overline{CEKE}\rangle$) versus global mean eddy kinetic energy ($\langle\overline{EKE}\rangle$). Regions where the depth of the ocean is shallower than 1,000 m are removed from the ratio estimation.

extensions and other energetic regions of the ocean contain both coherent and non-coherent components of the KE.

EKE is known to be more than an order of magnitude greater than KE of the mean flow (MKE; Gill et al., 1974); this result is clearly shown in Figure 3a, which indicates that $\overline{EKE}$ is responsible for almost all the $\overline{KE}$ across the ocean, except for regions with persistent currents over time. Such regions are the mean locations of WBC extensions, the equatorial Pacific current system, and regions in the Antarctic Circumpolar Current, where the $\overline{EKE}$ explains around 40% of the $\overline{KE}$. Chelton et al. (2011) estimated that time-tracked eddies with lifetimes greater than 4 weeks contain between 40% and 60% of the $\overline{EKE}$. Our method to reconstruct the spatially coherent eddy signature (Figure 3b) further corroborates that the coherent eddy component ($\langle\overline{CEKE}\rangle$) has ∼48% of the $\langle\overline{EKE}\rangle$ (Figure 3d). Although intuitively CS13 data set, being a subset from the spatially coherent eddies, could be expected to have less energy, the estimate presented in Chelton et al. (2011) extracts the total geostrophic velocity within a circle of radius encompassing each detected coherent eddy; thus this estimate contains more energy as it does not differentiate between the energy of coherent eddies and other processes. In contrast, MM19 only estimates the energy of the spatially coherent eddies by using the geostrophic approximation on each Gaussian imprint. The fact that these results are consistent is evidence that large long-lived eddies dominate the climatological energy of the spatially coherent eddy field. Furthermore, global area averages of the ratios show that $\langle\overline{EKE}\rangle$ explains ∼79% of the ocean $\langle\overline{KE}\rangle$ field, while non-coherent eddy features contain ∼57% percent of the $\langle\overline{EKE}\rangle$. Note that the globally averaged coherent and non-coherent components do not add to 100% as the cross terms ($\mathcal{O}_c$) are non-zero and can be interpreted as the error of the spatially coherent eddy reconstruction (±5%). The spatial pattern reveals a dominance of the $\overline{CEKE}$ equatorward from the WBC extensions and in areas with large coherent eddy contributions of around 80% of the region's EKE, such as the Southeast Indian Ocean, the Tehuantepec Gulf, and the tropical Atlantic. Another apparent signal is a reduction of the energy contained by coherent eddies at high latitudes and an increase in the energy explained by non-coherent eddies. This signal could be a consequence of the inability of the 0.25° gridded satellite altimetry to resolve coherent eddies with scales smaller than ∼25 km (first baroclinic Rossby radius at 60°; Chelton et al., 1998), as the effective resolution of the satellite gridded data set is ∼25 km at high latitudes and ∼200 km near the Equator (Ballarotta et al., 2019).

Figure 4 shows the seasonal cycle of the area-weighted EKE and CEKE for the Northern Hemisphere ($\langle EKE\rangle_{NH}$ and $\langle CEKE\rangle_{NH}$; 10°N–60°N) and Southern Hemisphere ($\langle EKE\rangle_{SH}$ and $\langle CEKE\rangle_{SH}$; 60°S–10°S). In both hemispheres, the $\langle EKE\rangle$ and $\langle CEKE\rangle$ peak during summer, consistent with Uchida et al. (2017), where scales larger than 100 km have the highest KE in summertime. In the Northern Hemisphere, the largest $\langle EKE\rangle_{NH}$ and $\langle CEKE\rangle_{NH}$ occurs in July, ∼6 months after the maximum winds in January (purple bar and black star in Figures 4c and 4d). Meanwhile, the Southern Ocean $\langle EKE\rangle_{SH}$ and $\langle CEKE\rangle_{SH}$ seasonal maxima arise during December, ∼4 months after the maximum winds in August (purple bar and back star in Figures 4g, and 4h). This lag between winds and the eddy and spatially coherent eddy energy components is further discussed in Section 3.2.

Panels a, b, e, and f in Figure 4 show the temporal evolution of $\langle EKE\rangle$ and $\langle CEKE\rangle$. Note that high frequency variability can be observed in the $\langle CEKE\rangle$ field with temporal scales of a few months, this variability could be attributed to regional dynamics averaged over the hemisphere (boundary currents, ocean gyres, etc.), as well as errors within the spatially coherent eddy reconstruction. Figure 4 also highlights long-term changes of the seasonal cycle and interannual variability over the record. For example, the Northern Hemisphere winters during

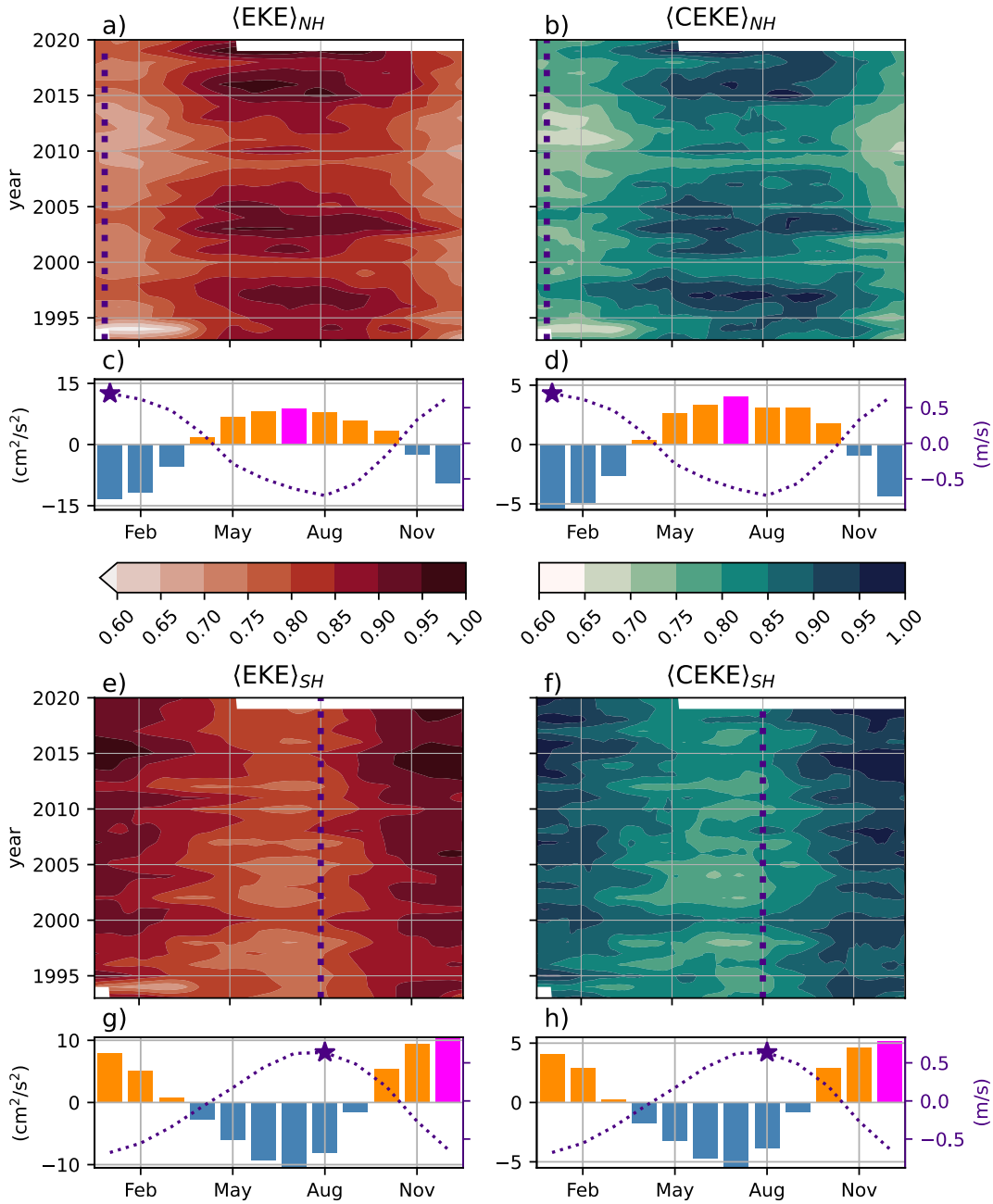

Figure 4. Seasonality of the normalized area-weighted eddy kinetic energy (⟨EKE⟩; $cm^2\ s^{-2}$) and spatially coherent eddy kinetic energy (⟨CEKE⟩; $cm^2\ s^{-2}$). Panels (a, b) show the Northern Hemisphere, while panels (e, f) correspond to the Southern Hemisphere. Panels (c, d) show the seasonal cycle anomaly of the $\langle EKE \rangle_{NH}$ and $\langle CEKE \rangle_{NH}$ in the Northern Hemisphere, and panels (g, h) show the Southern Hemisphere $\langle EKE \rangle_{SH}$ and $\langle CEKE \rangle_{SH}$. Bars correspond to the seasonal cycle anomaly of the fields and dotted purple lines show the climatological mean anomaly over 1993–2015 of the wind magnitude, smoothed with a 120 days running average.

early years of the record had a more energetic coherent eddy field, which has transitioned to a weaker CEKE field since 2010, in other words, the intensity of the $\langle CEKE \rangle_{NH}$ field has decreased. Another long-term change can be observed in the Southern Hemisphere, where intensity over time in $\langle EKE \rangle_{SH}$ and $\langle CEKE \rangle_{SH}$ supports the previously observed strengthening of the eddy field in the Southern Ocean (Hogg et al., 2015; Martínez-Moreno et al., 2019, 2021).

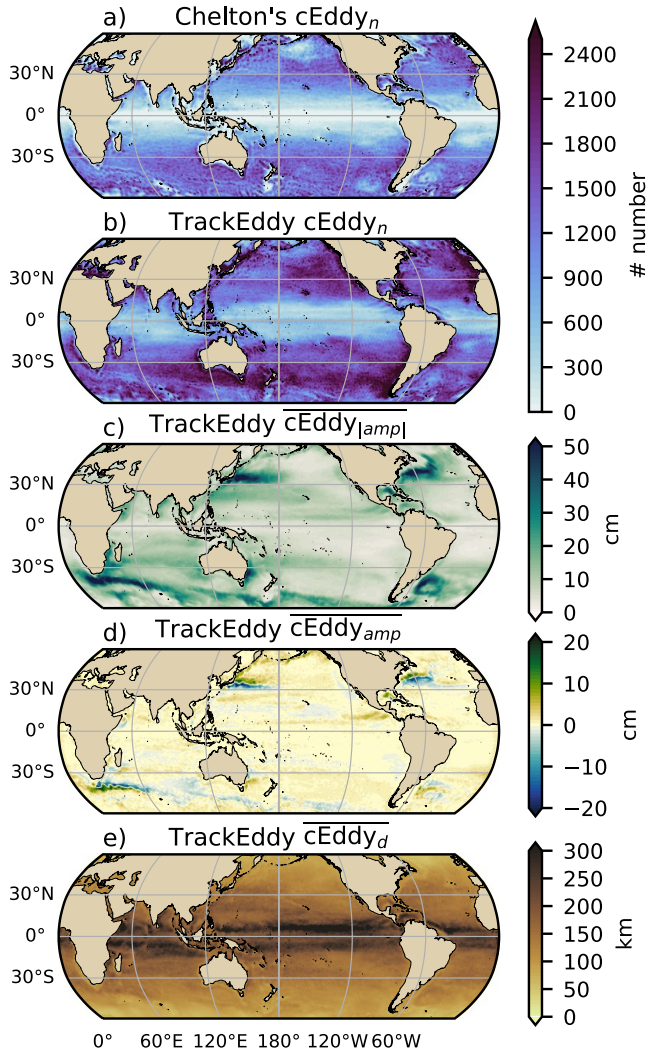

Figure 5. Averaged spatially coherent eddy statistics. (a) Climatology of the number of time-tracked eddies (cEddy$_n$) identified by Chelton et al. (2007); (b) Climatology of the number of spatially coherent eddies (cEddy$_n$) identified by Martínez-Moreno et al. (2019); (c) Climatology of the mean absolute coherent eddy amplitude (cEddy$_{amp}$), (d) Climatology of the mean coherent eddy amplitude (cEddy$_{amp}$), and (e) Climatology of the mean coherent eddy diameter (cEddy$_d$).

3.2. Global Spatially Coherent Eddy Statistics

Spatially CEKE allows us to quantify and study the energy of the eddy field, but the coherent eddy properties computed by automated coherent eddy identification algorithms allow us to further investigate temporal changes of their abundance (i.e., the number of eddies) and their intensity (both their amplitude and diameter). Figure 5 shows gridded estimates of the number of eddies and the eddy amplitude. In this analysis, we contrast our MM19 eddy count with that of CS13 (Chelton et al., 2007, Figures 5a and 5b). Although the number of identified eddies is larger in MM19, possibly due to the lifespan filter implemented by CS13, both datasets reveal consistent spatial patterns. For example, both datasets show an important meridional variation in the abundance of eddies, with high numbers of eddies in mid-latitudes and fewer eddies in the tropics and at high-latitudes (~60°). Additionally, there is a tendency at mid-latitudes (30°) for higher numbers of eddies in the eastern side of ocean basins (e.g., the East North Pacific, East North Atlantic, East South Pacific, and East South Atlantic). Another interesting pattern emerges in both eddy count datasets, where the eddy count field shows granularity. This granularity suggests a preferential match between the paths of time-tracked and spatially coherent eddies at boundary current extensions and over regions of the Southern Ocean. These structures and paths of coherent eddies could be associated with topographic features, with overall consistency between the eddy count patterns using the two different eddy identification methods.

Several regions such as the eastern side of mid-latitude ocean basins present large counts of eddies with small amplitudes (Figure 5c), for example, the eastern side of mid-latitude ocean basins. The ocean gyre interiors have a larger absolute amplitude and finally regions such as the boundary current extensions and the Antarctic Circumpolar Current have the largest spatially coherent eddy absolute amplitudes, as also shown by Chelton et al. (2011). Eddy amplitude highlights regions dominated by a given coherent eddy polarity, for example, boundary current extensions have a preferred sign (Figure 5d); namely, positive amplitude polewards of the WBC extension mean location, and negative amplitude equatorwards. This sign preference is consistent with the way that coherent eddies are shed from boundary current extensions; with positive eddy amplitudes poleward and negative eddy amplitudes equatorward of the WBC extension (Chelton et al., 2007, 2011; Kang & Curchitser, 2013). These global statistics reveal the absolute coherent eddy amplitude as a proxy for the CEKE with similar spatial patterns (Figures 2 and 5c) and showcases that in regions where $\overline{\text{CEKE}}$ accounts for a large proportion of $\overline{\text{EKE}}$ (Figure 3), the absolute coherent eddy amplitude is also large. The eddy diameter varies with latitude, where the largest eddies are located near the Equator (Figure 5e). More importantly, as noted by Chelton et al. (2011) and Stammer (1998), scales of observed mesoscale eddies are larger than the Rossby radius at mid and high latitudes; this observation is consistent with the inverse energy cascade.

3.3. Trends

Trends of EKE have been observed over the satellite record (Hogg et al., 2015; Martínez-Moreno et al., 2021), where overall the eddy-rich regions have increased the most. Here, we explore the long-term readjustment of the spatially coherent eddy properties including the number of coherent eddies, the absolute coherent eddy amplitude, and the coherent eddy amplitude polarities (Figure 6). To corroborate the previously observed trends, we first compare the trends from the MM19 and CS13 datasets. Note that both datasets show consistent spatial patterns and magnitude of the trends of the number of coherent eddies and the absolute coherent eddy amplitude. Spatial patterns can be observed in the Southern Ocean, North Atlantic and North Pacific where an increase in

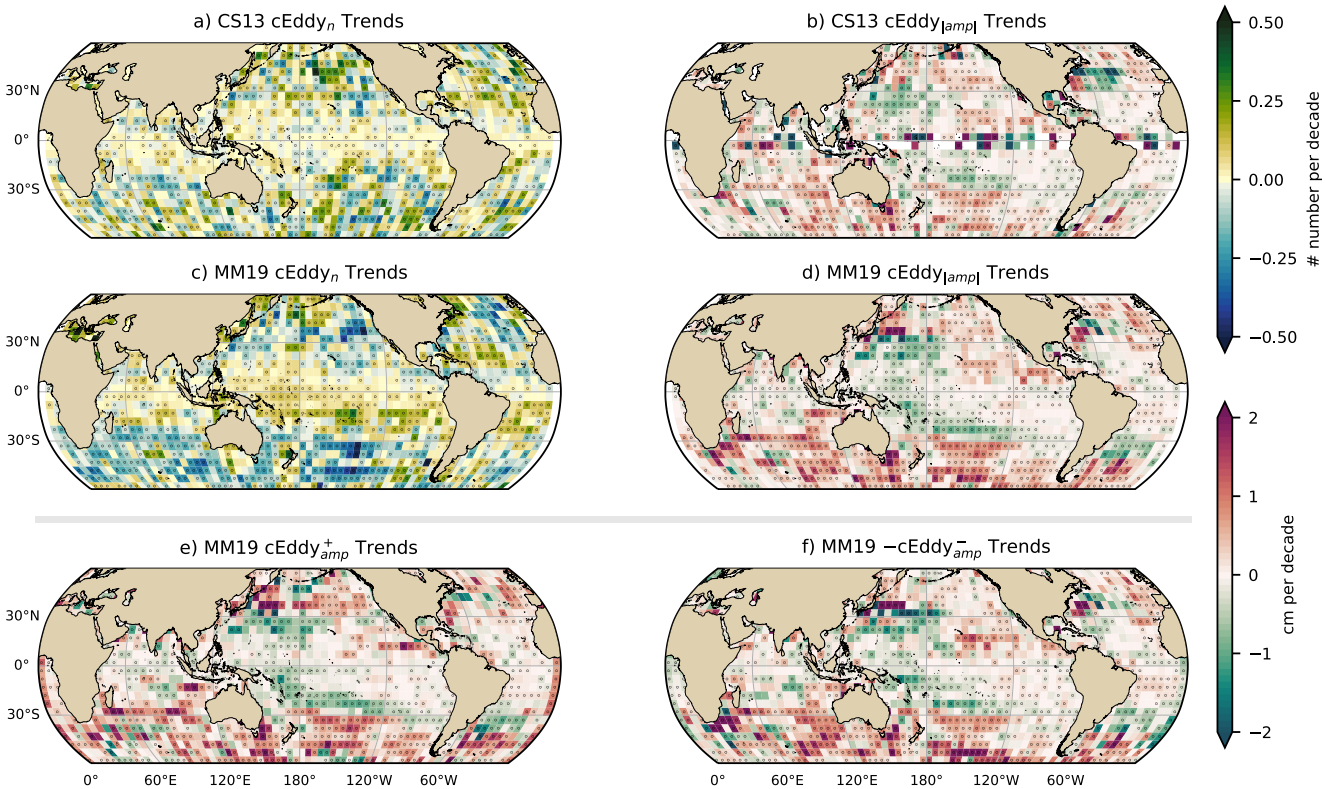

Figure 6. Trends of spatially coherent eddy statistics. (a, c) trends of the number of identified time-tracked and spatially coherent eddies from satellite observations identified in CS13's data set and MM19, respectively. (b, d) trends of the absolute value of identified spatially coherent eddy amplitude (cEddy$_{|amp|}$) from satellite observations reported by CS13 and MM19. (e, f) trends of the eddy amplitude polarity using MM19 (cEddy$^+_{amp}$ and cEddy$^-_{amp}$). Gray stippling shows regions that are statistically significant above the 95% confidence level.

the absolute coherent eddy amplitude is colocated with a decrease in the number of eddies. These regions with some of the largest changes in coherent eddy amplitude are consistent with those observed in mesoscale EKE (Martínez-Moreno et al., 2021) and provide additional evidence of a readjustment of the mesoscale eddy field and spatially coherent mesoscale eddy field over the last 3 decades.

The trends of cEddy$_{|amp|}$ in several oceanic regions have the same scale as sea level rise (∼2 cm per decade). To remove the trends that may come from sea level rise, we analyze each coherent eddy amplitude polarity. Both positive and negative coherent eddy amplitude have intensified in the Southern Ocean and North East Pacific and Atlantic. In other words, the amplitudes of each polarity has increased over time, and thus this strengthening is an intrinsic response of the coherent eddy field (Figures 6e and 6f).

3.4. Seasonality of Spatially Coherent Eddy Properties

To further understand the seasonal cycle of ⟨CEKE⟩, we compute the climatology of spatially coherent eddy properties in each hemisphere (Figure 7). The seasonal maxima of the number of eddies occurs in spring; in the Northern Hemisphere the maxima takes place during April (Figures 7a and 7c), while the Southern Hemisphere maximum occurs during October (Figures 7e and 7g). Meanwhile, the seasonal maxima of the eddy amplitude $\left(\left\langle \text{cEddy}_{|amp|} \right\rangle\right)$ occur during summer; peaking in September for the Northern Hemisphere and January in Southern Hemisphere (Figures 7b, 7d and 7f, and 7h). As expected, the seasonality of $\left\langle \text{cEddy}_{|amp|} \right\rangle$, which is equivalent to the intensity of the coherent eddies, coincides with the seasonal cycle of ⟨CEKE⟩.

A key feature of Figure 7 is a distinct lag of ∼3 months between the winds and eddy count, while the eddy amplitude maximum occurs ∼6 months after the seasonal maximum in winds. We hypothesize that the eddy number is out of phase with an increase in the spatially coherent eddy amplitude due to the inverse energy cascade where energy is transferred to larger scales through eddy-eddy interactions (e.g., due to merging of

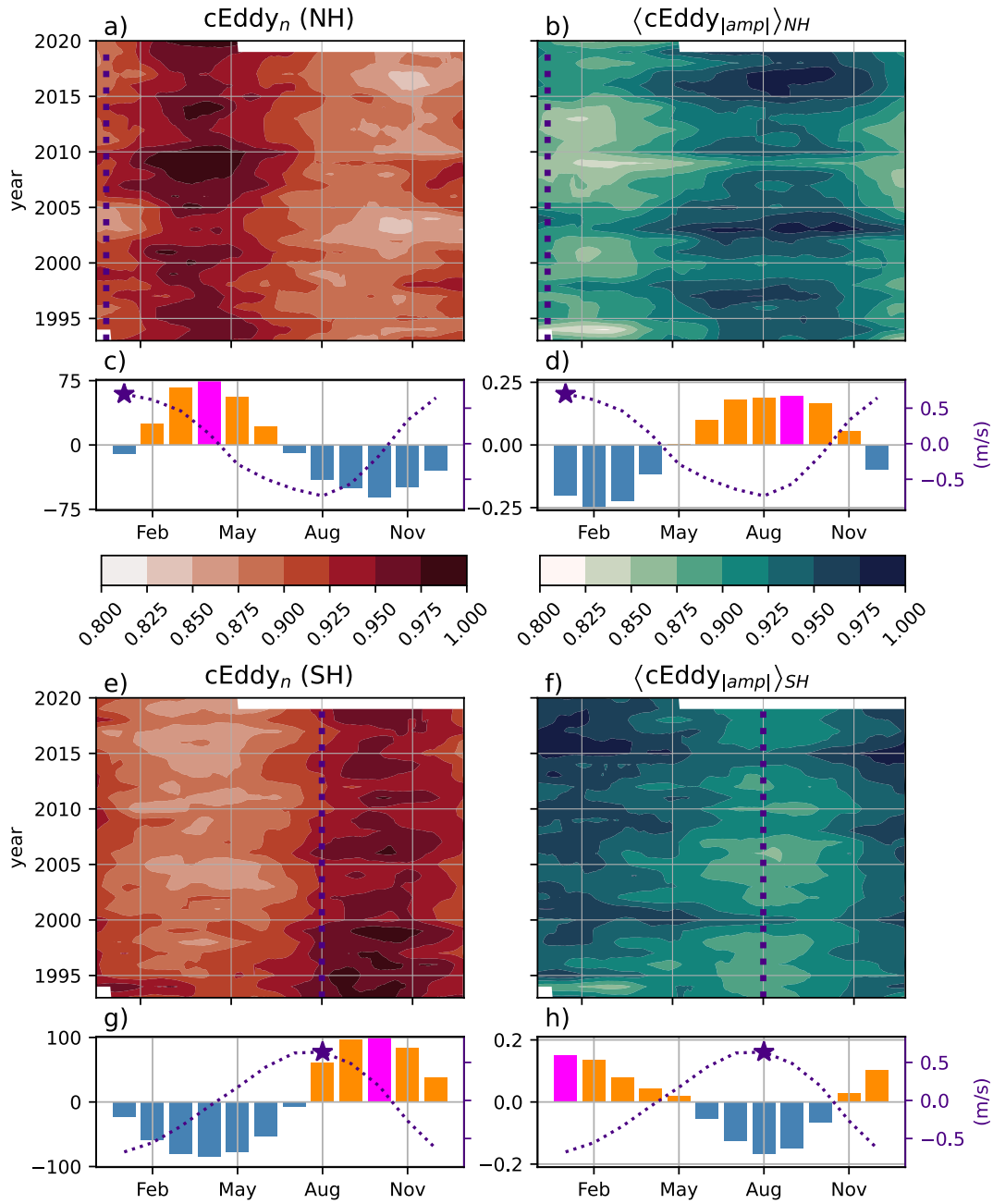

Figure 7. Seasonality of the normalized count of number of eddies (cEddy$_n$) and the area-weighted polarity independent spatially coherent eddy amplitude ($\langle \text{cEddy}_{amp} \rangle$; cm); Panels (a, b) show the Northern Hemisphere, while panels (e, f) correspond to the Southern Hemisphere. Panels (c, d) show the seasonal cycle of cEddy$_n$ and $\langle \text{cEddy}_{|amp|} \rangle_{NH}$ in the Northern Hemisphere, and panels (g, h) show the Southern Hemisphere, cEddy$_n$ and $\langle \text{cEddy}_{|amp|} \rangle_{SH}$. Bars correspond to the seasonal cycle anomaly of the fields and dotted purple lines show the climatological mean anomaly over 1993–2015 of the wind magnitude, smoothed with a 120 days running average.

coherent eddies). Furthermore, the observed seasonal lags and summer maximum is consistent with previous studies which suggest that a time-lag of the inverse cascade (Qiu et al., 2014; Sasaki et al., 2014) is responsible for the EKE seasonal cycle. These studies report that during spring, features with scales of 50–100 km have the highest EKE, while larger scales (>100 km; Uchida et al., 2017) are the most energetic during summertime. Smaller scales (<50 km; non-resolvable with satellite observations) have the highest EKE during winter. The maximum

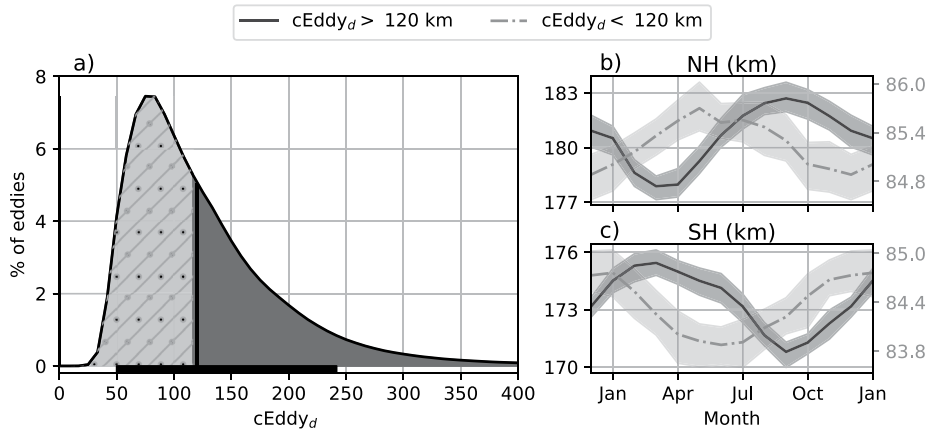

Figure 8. Distribution of the identified eddy diameter (cEddy$_d$; km) and hemispherical seasonality of the spatially coherent eddy diameter. (a) Distribution in percentage of identified eddy amplitude, solid bar below distribution represents 90% of the identified eddies. Seasonal cycle of the eddy diameter for the (b) Northern Hemisphere and (c) Southern Hemisphere. Dark solid line in panels (b, c), and dark shaded areas in panel (a) corresponds to spatially coherent eddies with diameters larger than 120 km, while light gray dash-dotted line in (b, c), and hatched area in (a) shows spatially coherent eddies with diameters smaller than 120 km. Gray envelope in (b, c) show seasonal changes in 100 randomly sub-samples of 1% of the data ($n \sim 345{,}000$).

of ⟨EKE⟩, ⟨CEKE⟩, and $\langle \text{cEddy}_{|amp|} \rangle$ coincides with summertime is partial evidence that the seasonality of eddies and coherent eddies could be dictated by the inverse energy cascade and dominated by scales larger than 100 km.

This hypothesis can be further explored by looking at the seasonal evolution of the eddy diameter (cEddy$_d$). Note that 90% of identified spatially coherent eddies have diameters between 50 and 220 km (Figure 8a). We partition eddies into large-scale coherent eddies (diameter >120 km) and small-scale coherent eddies (diameter <120 km; Figure 8a). In the Northern Hemisphere, small-scale coherent eddies have a seasonal peak in diameter by the end of spring (May), while large-scale coherent eddies have the greatest diameter in early autumn (September; Figure 8b). Meanwhile, in the Southern Hemisphere, the small-scale coherent eddies exhibit maximum diameter in early summer (December), while the diameter of large-scale coherent eddies peaks in late summer (February; Figure 8c). The maxima of the different coherent eddy scales suggests that wind energy provided to the mean flow generates small coherent eddies via baroclinic instability early in the season, which then merge and grow to become larger in diameter and amplitude, and thus, more energetic. This is consistent with the inverse energy cascade, and suggests that this mechanism not only drives EKE seasonality, but also may be responsible for the seasonal cycle of coherent eddies.

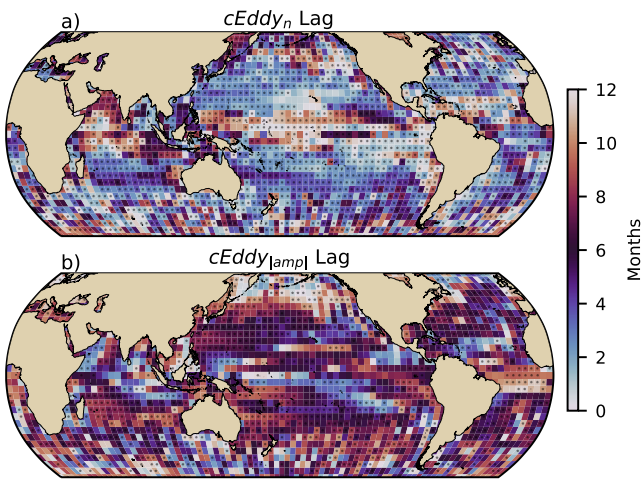

Figure 9. Time-lagged correlation between the wind magnitude of climatology year and (a) number of eddies (cEddy$_n$) and (b) eddy amplitude (cEddy$_{|amp|}$), gridded in four by 4° boxes. Stippling shows the significance above 95% confidence level.

3.5. Regional Climatology

Time-lagged correlations provide a way to characterize the spatial patterns of the lags between the spatially coherent eddy properties and the winds. Figure 9 shows the lag between climatological years of the number of eddies, eddy amplitude and the wind magnitude. The spatial pattern of Figure 9 in regions such as the WBCs and ocean gyre interiors show a lag of a few months between the number of eddies and the maximum winds, while the eddy amplitude is out of phase with the winds in those same regions. Due to this spatial dependence, regions with large CEKE are further investigated. A summary of the time-lag, correlations coefficients, and ratios for regions with large CEKE; Gulf Stream, Kuroshio Current, Agulhas Current, south-east Indian Ocean, and East Tropical Pacific are presented in Table 1.

The most energetic WBCs include the Gulf Stream, the Kuroshio Current, and the Agulhas Current; using different extends for each region yielded similar qualitative and quantitative results (Figures 10–12). Spatially coherent eddy generation in boundary current extensions occurs through baroclinic

Table 1
Lagged Correlations Between Spatially Coherent Eddy Statistics and Wind Magnitude, Averaged Ratio of the EKE Contained in CEKE for Regions With Large Concentrations of CEKE

Region (coordinates)	$cEddy_n$		$\langle cEddy^+_{amp} \rangle$		$\langle cEddy^-_{amp} \rangle$		Ratio (%)	Correlation $cEddy_n$ and $cEddy_{\lvert amp \rvert}$
	Correlation	Lag (months)	Correlation	Lag (months)	Correlation	Lag (months)		
Gulf Stream (80°W–39°W, 25°N–38°N)	0.98	2.6	0.99	6.2	0.99	7.6	55.85	−0.56
Kuroshio Current (125°E−166°E, 23°N–36°N)	0.99	2.6	0.98	7.1	0.97	6.8	56.49	−0.54
Agulhas Current (20°E−61°E, 27°S–40°S)	0.98	1.3	0.98	4.3	0.96	6.7	56.45	−0.38
Southeast Indian Ocean (85°E−126°E, 31°S–44°S)	0.99	1.7	0.75	0.2	0.94	2.7	65.82	−0.59
East Tropical Pacific (130°W–89°W, 7°N–20°N)	0.85	3.8	0.90	0.4	0.63	6.3	58.17	−0.45

and barotropic instabilities of the mean current, thus all these regions share similar eddy-generation dynamics. In all these regions without exception: (a) CEKE contains 55%–65% of the EKE in regions equatorward from the mean WBC extensions, (b) the number of eddies is consistently small over the mean WBC extensions, and (c) the eddy amplitude is larger over the mean WBC extensions than in surrounding regions.

In the Gulf Stream, the energy ratio between coherent and total EKE is ∼56% (Figure 10). The highest energy ratio occurs in regions with numerous eddies, colocated with regions where the largest $cEddy_{\lvert amp \rvert}$ gradients occur. The time series of $cEddy_n$ and $\langle cEddy_{\lvert amp \rvert} \rangle$ are anti-correlated (−0.55; Figure 10b), and they display an important interannual and seasonal variability. Although Chaudhuri et al. (2009) observed that a positive phase of the North Atlantic Oscillation exhibits higher EKE, due to an increase in baroclinic instability, thus suggesting more spatially coherent eddies, we do not find a correlation between the $cEddy_n$ or the $\langle cEddy_{\lvert amp \rvert} \rangle$ in the Gulf Stream and the North Atlantic Oscillation index. Similar to the signal observed in the hemispheric analysis, the eddy count seasonal cycle follows the wind maximum lagging by ∼3 months, while the amplitude of the coherent eddies lags by ∼6 months.

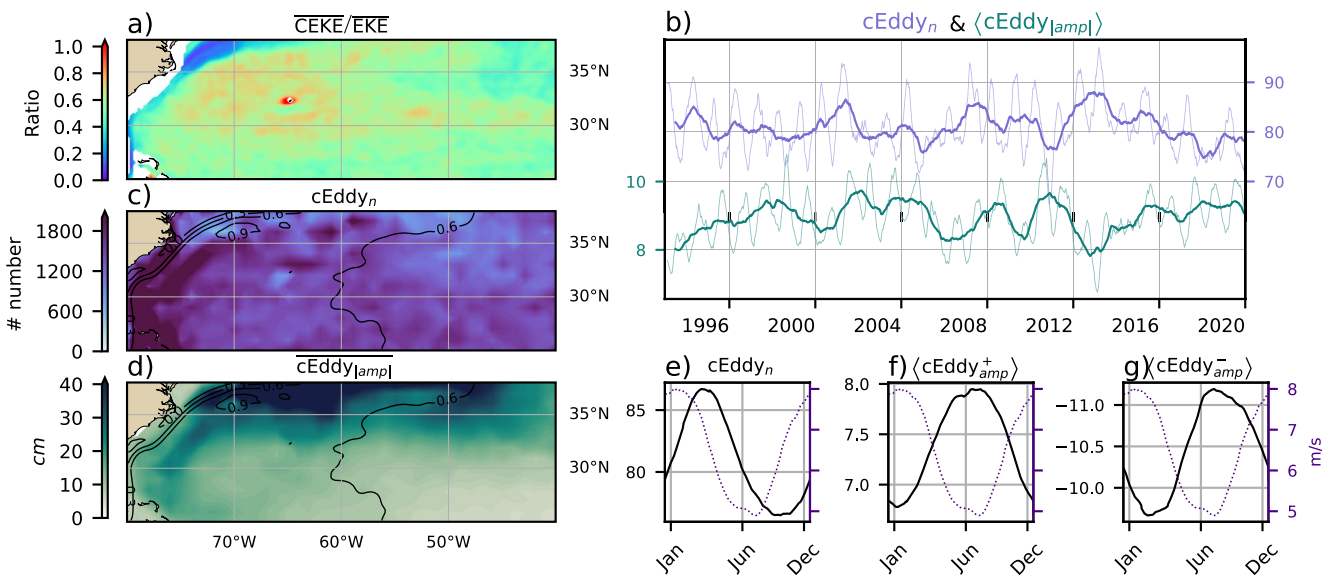

Figure 10. Climatology of the eddy field and spatially coherent eddy field in the Gulf Stream. (a) Ratio of mean spatially coherent eddy kinetic energy ($\overline{CEKE}$) vs. mean eddy kinetic energy ($\overline{EKE}$); (b) Thick lines show the running average over 2 years and thin lines show the running average over 90 days of the spatially coherent eddy number sum and the average coherent eddy amplitude; (c) Map of the number of eddies; (d) Map of the average coherent eddy amplitude; (e) Seasonal cycle of the number of eddies ($cEddy_n$); (f) Seasonal cycle of the positive coherent eddy amplitude ($\langle cEddy^+_{amp} \rangle$; m), and (g) Seasonal cycle of the negative coherent eddy amplitude ($\langle cEddy^-_{amp} \rangle$; m). Contours in maps correspond to mean sea surface height (m). Dotted lines show the seasonal cycle of the wind magnitude over the Gulf Stream between 1993 and 2020.

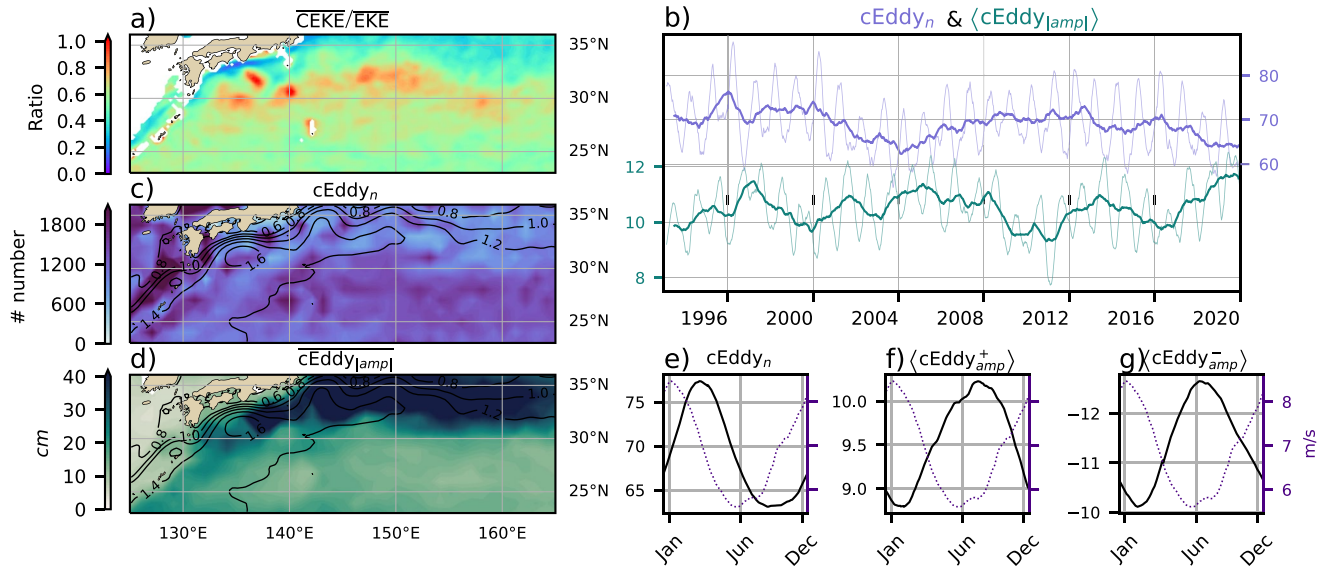

Figure 11. As in Figure 10, only showing the climatology of the eddy field and spatially coherent eddy field in the Kuroshio extension. (a) Ratio of mean coherent eddy kinetic energy ($\overline{\text{CEKE}}$) vs. mean eddy kinetic energy ($\overline{\text{EKE}}$); (b) Time-series of the coherent eddy number and the average coherent eddy amplitude; (c) Map of the number of eddies; (d) Map of the average coherent eddy amplitude; Seasonal cycle of the (e) number of eddies; (f) positive coherent eddy amplitude, and (g) negative coherent eddy amplitude. Dotted lines show the seasonal cycle of the wind magnitude over the Kuroshio extension between 1993 and 2020.

The time series of the cEddy$_n$ and $\langle \text{cEddy}_{|amp|} \rangle$ in the Kuroshio Current are weakly anti-correlated (−0.44; Figure 11b), but present important interannual variability possibly due to westward propagating Rossby waves associated to the North Pacific Oscillation (Wang & Tang, 2022). However, on average 58% of the energy in the region corresponds to CEKE. As observed in the Gulf Stream, there is an important seasonal cycle in the boundary current extension, where the maximum of the seasonal cycle of the eddy count occurs in March, lagging the wind maximum by ∼3 months (January). Meanwhile, the amplitude of the spatially coherent eddies lags the wind maximum by ∼6 months (June).

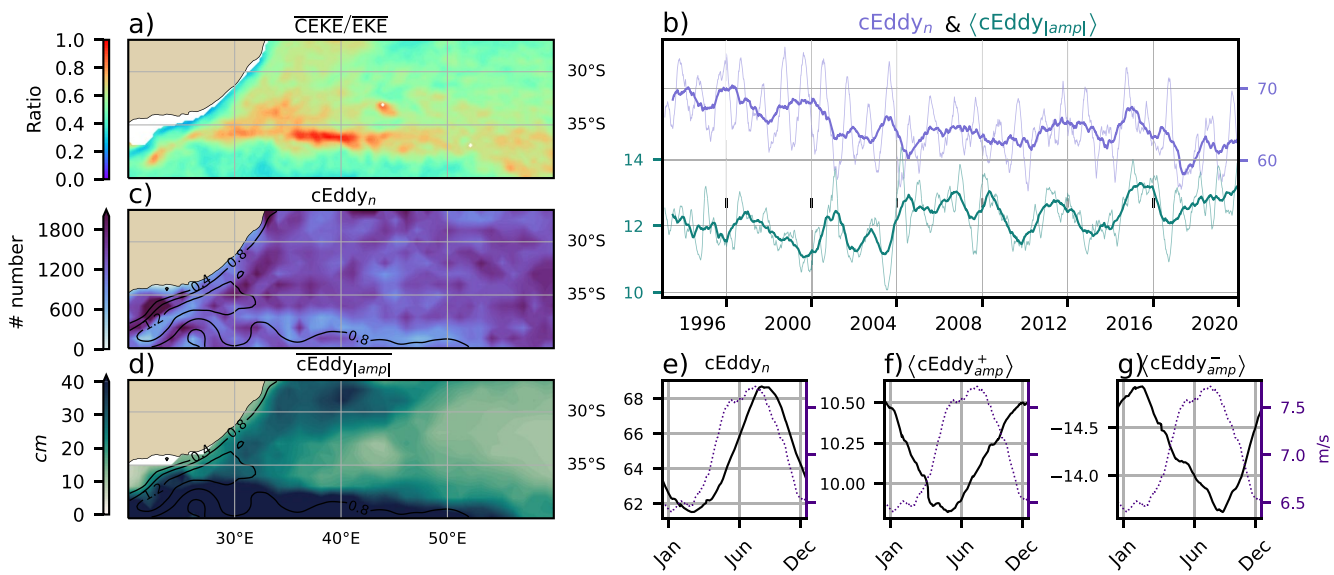

Figure 12. As in Figure 10, only showing the climatology of the eddy field and spatially coherent eddy field in the Agulhas Current. (a) Ratio of mean coherent eddy kinetic energy ($\overline{\text{CEKE}}$) vs. mean eddy kinetic energy ($\overline{\text{EKE}}$); (b) Time-series of the coherent eddy number and the average coherent eddy amplitude; (c) Map of the number of eddies; (d) Map of the average coherent eddy amplitude; Seasonal cycle of the (e) number of eddies; (f) positive coherent eddy amplitude, and (g) negative coherent eddy amplitude. Dotted lines show the seasonal cycle of the wind magnitude over the Agulhas Current between 1993 and 2020.

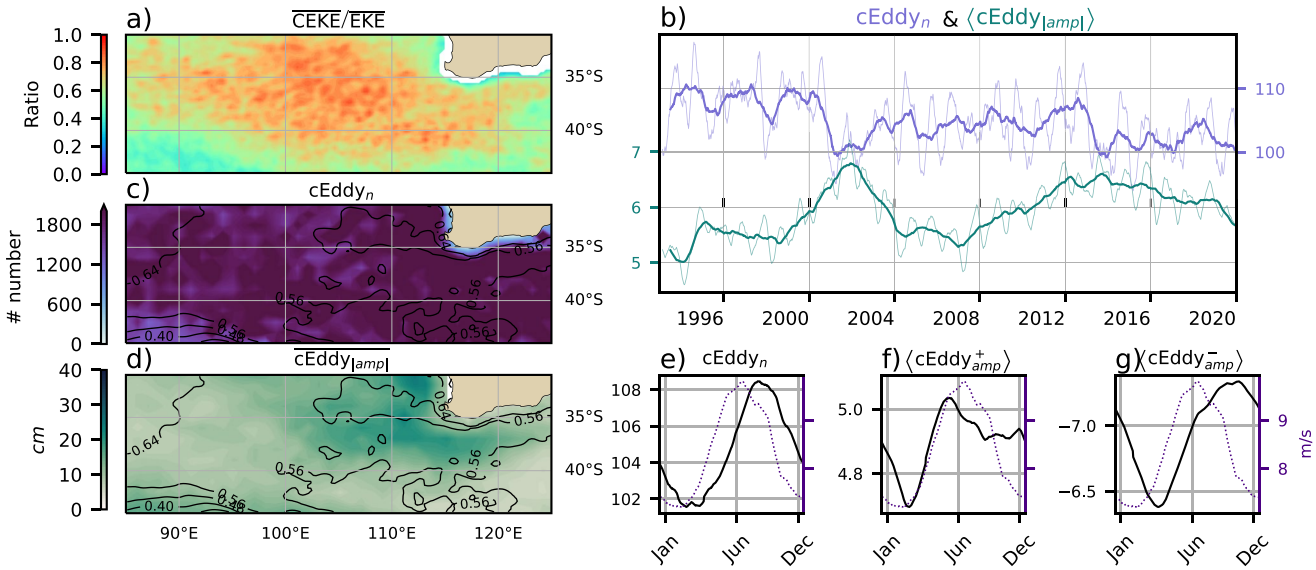

Figure 13. As in Figure 10, only showing the climatology of the eddy field and spatially coherent eddy field in the southeast Indian Ocean. (a) Ratio of mean coherent eddy kinetic energy ($\overline{\text{CEKE}}$) vs. mean eddy kinetic energy ($\overline{\text{EKE}}$); (b) Time-series of the coherent eddy number and the average coherent eddy amplitude; (c) Map of the number of eddies; (d) Map of the average coherent eddy amplitude; Seasonal cycle of the (e) number of eddies; (f) positive coherent eddy amplitude, and (g) negative coherent eddy amplitude. Dotted lines show the seasonal cycle of the wind magnitude over the southeast Indian Ocean between 1993 and 2020.

In the Southern Hemisphere the strongest boundary current, the Agulhas Current, shows similar behavior to its counterparts in the Northern Hemisphere (Figure 12). On average, spatially coherent eddies in the Agulhas Current contain ∼62% of the energy. Over the satellite record, large interannual variability can be observed (Figure 12b), however there is no strong anticorrelation between the cEddy$_n$ and $\langle \text{cEddy}_{|amp|} \rangle$ as boundary currents in the northern hemisphere. The seasonal peak of cEddy$_n$ occurs in August, while the $\langle \text{cEddy}_{|amp|} \rangle$ peak occurs in January–February. The seasonal lag between the winds, eddy count, and eddy amplitude in each of the WBC extensions is interpreted as being analogous to the lagged response of coherent eddy properties (Figure 7) due to eddy-eddy interactions, consistent with the inverse cascade of energy.

Spatially coherent eddies dominate the EKE field in other regions such as the southeast Indian Ocean (Figure 13), where 65% of the energy is contained in large and abundant coherent eddies. The interannual variability shows an anti-correlation of −0.59 (Figure 13b) and displays important interannual variability possibly due to the variability of the EKE associated to ENSO through the modulation of baroclinic instability in the region (Zheng et al., 2018). The time-series reveal a significant increase in the $\langle \text{cEddy}_{|amp|} \rangle$, while the cEddy$_n$ has decreased over the last 3 decades. The seasonal cycle shows that the cEddy$_n$ peak occurs in August, 3 months after the maximum winds (June). Meanwhile, the $\langle \text{cEddy}^+_{amp} \rangle$ responds in synchrony to the winds, and the $\langle \text{cEddy}^-_{amp} \rangle$ is in phase with the seasonal cycle of the eddy number (cEddy$_n$). Hence, this region contrasts with the behavior of WBC extensions, and suggests spatial variability and different forcing mechanisms, such as MLD seasonality and seasonality of baroclinic instability, may drive the seasonal cycle of coherent eddies.

Another region with important contributions to the spatially coherent eddy field is the East Tropical Pacific (Tehuantepec region; Figure 14), where coherent eddies contain ∼56% of the energy. In fact, coherent eddy generation in this region is modulated by winds and coastally trapped waves which produce a strong horizontal and vertical shear (baroclinic and barotropic instabilities; Trasviña et al., 1995; Zamudio et al., 2006; Willett et al., 2006). Furthermore, the equatorial generated waves propagating along the coast have an important interannual variability observable in the $\langle \text{cEddy}_{|amp|} \rangle$ time-series, where El Niño events are notable during 1997 and 2015 (Figure 14b). The seasonal cycle of cEddy$_n$, $\langle \text{cEddy}^+_{amp} \rangle$, and $\langle \text{cEddy}^-_{amp} \rangle$ supports the idea of a coherent eddy response to two different coherent eddy generation mechanisms; the number of eddies lags by ∼3 months from the winds. While, the $\langle \text{cEddy}^+_{amp} \rangle$ is in phase with the winds and the time of maximum trapped wave activity (winter; Zamudio et al., 2006), the $\langle \text{cEddy}^-_{amp} \rangle$ is out of phase with the wind magnitude possible due to eddy-eddy interactions.

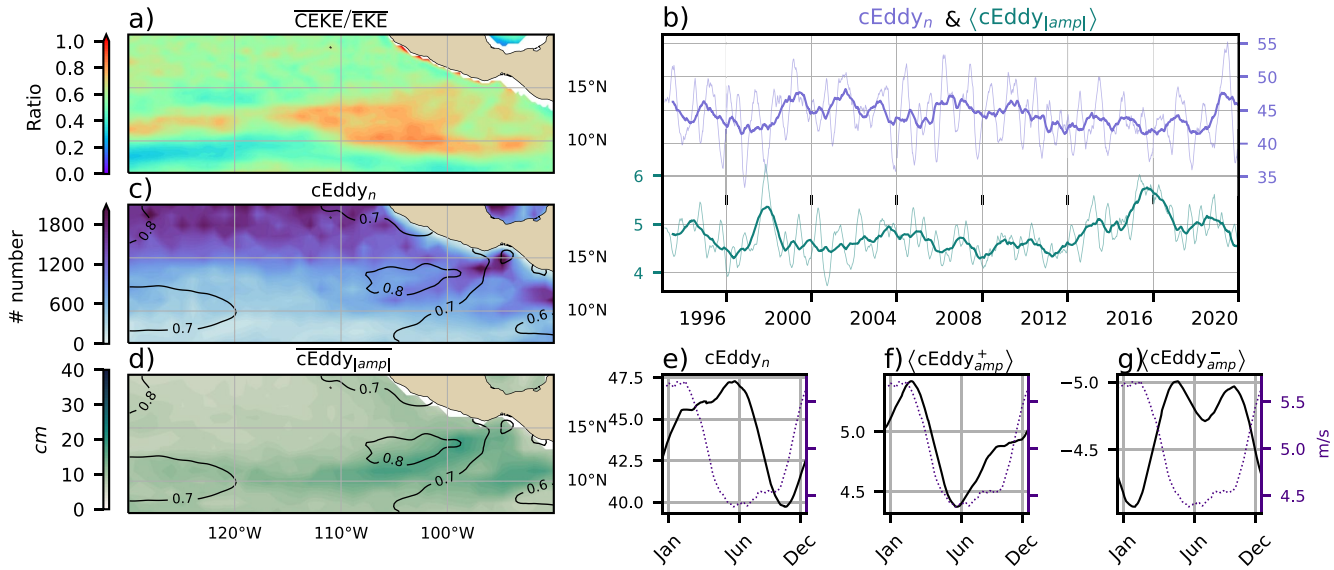

Figure 14. As in Figure 10, only showing the climatology of the eddy field and spatially coherent eddy field in the East Tropical Pacific. (a) Ratio of mean coherent eddy kinetic energy ($\overline{CEKE}$) vs. mean eddy kinetic energy ($\overline{EKE}$); (b) Time-series of the coherent eddy number and the average coherent eddy amplitude; (c) Map of the number of eddies; (d) Map of the average coherent eddy amplitude; Seasonal cycle of the (e) number of eddies; (f) positive coherent eddy amplitude, and (g) negative coherent eddy amplitude. Dotted lines show the seasonal cycle of the wind magnitude over the East Tropical Pacific between 1993 and 2020.

4. Discussion and Conclusions

The contribution of spatially coherent eddies to the total surface KE field from available satellite observations is estimated to be ∼48% of the total EKE. This half is concentrated in eddy-rich regions, where a recent multi-decadal intensification of the eddy field has been observed (Martínez-Moreno et al., 2021). Chelton et al. (2011) estimated the energy contained by time-tracked eddies with lifetimes of 4 weeks and longer to be ∼50%, comparable to those of this study using the spatially coherent eddy identification algorithm proposed in Martínez-Moreno et al. (2019). The main differences between these methods are the identification criteria of coherent eddies and how each study estimates the CEKE component. While, MM19 computes EKE from a reconstructed SSHa for only spatially coherent eddies, CS13 extracts the EKE within each time-tracked eddy closed contour. Additionally, different filters to reduce misidentification of time-tracked eddies are applied; MM19 discards features where the 2D Gaussian fit skill is below 90%, while CS13 apply lifespan and amplitude filters. These latter filters implemented by CS13 are widely used to track individual eddies in space and time. However, a lifespan filter can obscure interactions between eddies in energetic regions, where coherent eddies may interact with each other or merge into meanders and therefore have a shorter lifespan. Because of this, lifespan filters are not used in this study. More research is needed to minimize the errors associated with regions that have strong interactions between different mesoscale features (e.g., eddy-eddy and eddy-meander interactions).

It should also be noted that regions with first baroclinic Rossby radius of deformation smaller than 25 km cannot be resolved by satellite observations. Thus, the energy contained in coherent eddies around latitudes of 60° and those near the shore are missed from this estimate, and their role in the seasonal cycle and local dynamics remains unknown. New satellite altimeter missions (e.g., Surface Water and Ocean Topography; SWOT) may allow estimates of the energy contained in mesoscale coherent eddies outside the subtropical regions and over the continental slope.

Hemisphere-wide variability indicates a strong seasonal cycle of the EKE, CEKE, and coherent eddy properties. The seasonal cycle of the CEKE in each hemisphere is hypothesized to be a consequence of numerous small coherent eddies interacting with each other (eddy-eddy interactions) and resulting in stronger, larger and more energetic (but fewer) coherent eddies during summer, a few months after the yearly coherent eddy number maximum. This result is evidence of eddy-eddy interactions and thus the transfer of energy from smaller coherent eddies to larger coherent eddies (inverse energy cascade) could explain the observed seasonal cycle of CEKE and

coherent eddies properties. However, future research remains open to investigate the effects of the seasonal cycles of baroclinic and barotropic instabilities, as well as the seasonal cycle in mixed layer depth formation, in shaping the coherent eddy field using high-resolution models.

Spatially coherent eddy properties reveal a non-uniform long-term readjustment of the mesoscale eddy field. Overall, the eddy number has decreased globally at a significant rate of ∼35 eddies per decade from ∼4,000 eddies identified globally on average each day. Despite the small changes in the total eddy numbers, large proportions of the ocean show a major strengthening of the mesoscale coherent eddy amplitude at rates greater than ∼1 cm per decade. This strengthening of the coherent eddy amplitude is attributed to an intensification of each coherent eddy polarity, rather than a readjustment of the coherent eddy field to sea level rise. In other words, the coherent eddy amplitude intensification is occurring in both coherent eddy polarities and a proportion of the previously observed readjustments in the eddy field to long-term changes in the ocean forcing (Hu et al., 2020; Martínez-Moreno et al., 2021; Wunsch, 2020). This long-term readjustment reveals an intensification of the coherent eddy field, possibly due to long-term readjustments in the ocean baroclinic and barotropic instabilities, as well as the strength of the winds.

The reconstruction of the spatially coherent eddies and their statistics revealed regions with important coherent eddy contributions and a distinct seasonal evolution of the coherent eddies. WBC extensions generate eddies through the instability of the main currents and the seasonal cycle of coherent eddies. CEKE, and thus EKE could be associated with an inverse energy cascade observable through lagged seasonal cycles in the coherent eddy statistics (Table 1). The magnitude of the seasonal cycle amplitude in WBC extensions is two times larger than any other region, therefore, the seasonality of the coherent eddies in WBC extensions dominates the hemispheric seasonal cycle. The seasonal lag of the inverse energy cascade is coupled with the presence of fronts (Qiu et al., 2014), as in WBC extensions, and thus our results are consistent with the notion of baroclinic instability generating eddies and, via eddy-eddy interactions, a lagged inverse energy cascade.

The use of satellite observations in this study limits our ability to quantify the importance of the inverse energy cascade and other processes driving the spatially coherent eddy seasonal cycle. As mentioned above, there is evidence of an increase in eddy-eddy interactions, however we cannot discard important contributions from other processes such as the seasonal cycle of forcing, stratification, and instabilities, which are crucial in the generation of coherent eddies. We provide here a descriptive response of the coherent eddy field and further work is needed to assess the role of eddy-eddy interactions in our changing climate, ocean dynamics, and biogeochemical processes. The SWOT mission could allow us to advance our understanding of eddy-eddy interactions and the seasonal cycle of scales smaller than mesoscale may provide further evidence of the inverse energy cascade driving the coherent eddy seasonality. Current generation climate models have just started to resolve mesoscale dynamics, thus, the presented estimate of energy in spatially coherent eddies from satellite observations could be used as a benchmark that facilitates the evaluation of such models, and to quantify the energy contained by mesoscale and more specifically spatially coherent eddies in future climate projections. For example, a first step was undertaken by Samelson et al. (2019) to reconcile a stochastic model with a dynamical model and observations, however much remains to be done to include mesoscale eddies and their variability in climate models.

Acknowledgments
The Chelton and Schlax (2013) data set was produced by SSALTO/DUACS and distributed by AVISO+ (https://www.aviso.altimetry.fr/) with support from CNES, developed and validated in collaboration with E. Mason at IMEDEA. Our analysis were facilitated with the Python Packages; dask (Rocklin, 2015) and xarray (Hoyer & Hamman, 2017). We thank three anonymous reviewers for their comments that helped improve the clarity and structure of this paper. J. M.-M. was supported by the Consejo Nacional de Ciencia y Tecnología (CONACYT), Mexico funding. M. H. E. is supported by the Center for Southern Hemisphere Oceans Research (CSHOR), a joint research center between Qingdao National Laboratory for Marine Science and Technology (QNLM), Commonwealth Scientific and Industrial Research Organization (CSIRO), University of New South Wales (UNSW), and the University of Tasmania (UTAS). Analyses were undertaken on the National Computational Infrastructure in Canberra, Australia, which is supported by the Australian Commonwealth Government. Open access publishing facilitated by Australian National University, as part of the Wiley - Australian National University agreement via the Council of Australian University Librarians.

Data Availability Statement

Global spatially coherent eddy reconstruction, coherent and non-CEKE datasets, in addition to gridded spatially coherent eddy tracking datasets are publicly available at https://doi.org/10.5281/zenodo.4646429 (Martínez-Moreno et al., 2022). The updated data set of identified mesoscale eddies from Martínez-Moreno et al., (2019) can be down- loaded at http://dx.doi.org/10.25914/5cb6859e4df3e and https://doi.org/10.25914/CTWV-RK08. All analyses and figures in this manuscript are repro- ducible via Jupyter notebooks and instructions can be found in the Github repository CEKE_climatology (https://github.com/josuemtzmo/CEKE_climatology). Trends used the Python Package xarrayMannKendall (https://doi.org/10.5281/zenodo.4458776).

References

Amores, A., Jordà, G., Arsouze, T., & Sommer, J. (2018). Up to what extent can we characterize ocean eddies using present-day gridded altimetric products? *Journal of Geophysical Research: Oceans*, *123*(10), 7220–7236. https://doi.org/10.1029/2018JC014140

Arbic, B. K., Polzin, K. L., Scott, R. B., Richman, J. G., & Shriver, J. F. (2013). On eddy viscosity, energy cascades, and the horizontal resolution of gridded satellite altimeter products. *Journal of Physical Oceanography*, *43*(2), 283–300. https://doi.org/10.1175/jpo-d-11-0240.1

Ashkezari, M. D., Hill, C. N., Follett, C. N., Forget, G., & Follows, M. J. (2016). Oceanic eddy detection and lifetime forecast using machine learning methods. *Geophysical Research Letters*, *43*(23), 12234–12241. https://doi.org/10.1002/2016gl071269

Ballarotta, M., Ubelmann, C., Pujol, M.-I., Taburet, G., Fournier, F., Legeais, J.-F., et al. (2019). On the resolutions of ocean altimetry maps. *Ocean Science Discussions*, 1–27. https://doi.org/10.5194/os-2018-156

Beron-Vera, F. J., Wang, Y., Olascoaga, M. J., Goni, G. J., & Haller, G. (2013). Objective detection of oceanic eddies and the Agulhas leakage. *Journal of Physical Oceanography*, *43*(7), 1426–1438. https://doi.org/10.1175/JPO-D-12-0171.1

Bouali, M., Sato, O. T., & Polito, P. S. (2017). Temporal trends in sea surface temperature gradients in the South Atlantic Ocean. *Remote Sensing of Environment*, *194*, 100–114. https://doi.org/10.1016/j.rse.2017.03.008

Callies, J., Flierl, G., Ferrari, R., & Fox-Kemper, B. (2015). The role of mixed-layer instabilities in submesoscale turbulence. *Journal of Fluid Mechanics*, *788*, 5–41. https://doi.org/10.1017/jfm.2015.700

Cane, M. A., Clement, A. C., Kaplan, A., Kushnir, Y., Pozdnyakov, D., Seager, R., et al. (1997). Twentieth-century sea surface temperature trends. *Science*, *275*(5302), 957–960. https://doi.org/10.1126/science.275.5302.957

Chaudhuri, A. H., Gangopadhyay, A., & Bisagni, J. J. (2009). Interannual variability of Gulf Stream warm-core rings in response to the North Atlantic Oscillation. *Continental Shelf Research*, *29*(7), 856–869. https://doi.org/10.1016/j.csr.2009.01.008

Chelton, D. B., DeSzoeke, A. R., Schlax, M. G., Naggar, K., & Siwertz, N. (1998). Geographical variability of the first baroclinic Rossby radius of deformation. *Journal of Physical Oceanography*, *28*(3), 433–460. https://doi.org/10.1175/1520-0485(1998)028<0433:GVOTFB>2.0.CO;2

Chelton, D. B., & Schlax, M. G. (2013). Mesoscale eddies in altimeter observations of SSH.

Chelton, D. B., Schlax, M. G., & Samelson, R. M. (2011). Global observations of nonlinear mesoscale eddies. *Progress in Oceanography*, *91*(2), 167–216. https://doi.org/10.1016/j.pocean.2011.01.002

Chelton, D. B., Schlax, M. G., Samelson, R. M., & de Szoeke, R. A. (2007). Global observations of large oceanic eddies. *Geophysical Research Letters*, *34*(15), L15606. https://doi.org/10.1029/2007GL030812

CMEMS. (2017). The Ssalto/Duacs altimeter products were produced and distributed by the Copernicus Marine and Environment Monitoring Service. *Aviso Dataset*. Retrieved from https://www.aviso.altimetry.fr/

Cui, W., Wang, W., Zhang, J., & Yang, J. (2020). Identification and census statistics of multicore eddies based on sea surface height data in global oceans. *Acta Oceanologica Sinica*, *39*(1), 41–51. https://doi.org/10.1007/s13131-019-1519-y

Danabasoglu, G., McWilliams, J. C., & Gent, P. R. (1994). The role of mesoscale tracer transports in the global ocean circulation. *Science*, *264*(5162), 1123–1126. https://doi.org/10.1126/science.264.5162.1123

Dufour, C. O., Griffies, S. M., de Souza, G. F., Frenger, I., Morrison, A. K., Palter, J. B., et al. (2015). Role of mesoscale eddies in cross-frontal transport of heat and biogeochemical tracers in the Southern Ocean. *Journal of Physical Oceanography*, *45*(12), 3057–3081. https://doi.org/10.1175/JPO-D-14-0240.1

Faghmous, J. H., Frenger, I., Yao, Y., Warmka, R., Lindell, A., & Kumar, V. (2015). A daily global mesoscale ocean eddy dataset from satellite altimetry. *Scientific Data*, *2*(1), 150028. https://doi.org/10.1038/sdata.2015.28

Ferrari, R., & Wunsch, C. (2009). Ocean circulation kinetic energy: Reservoirs, sources, and sinks. *Annual Review of Fluid Mechanics*, *41*(1), 253–282. https://doi.org/10.1146/annurev.fluid.40.111406.102139

Frenger, I., Gruber, N., Knutti, R., & Münnich, M. (2013). Imprint of Southern Ocean eddies on winds, clouds and rainfall. *Nature Geoscience*, *6*(8), 608–612. https://doi.org/10.1038/ngeo1863

Frenger, I., Münnich, M., Gruber, N., & Knutti, R. (2015). Southern Ocean eddy phenomenology. *Journal of Geophysical Research: Oceans*, *120*(11), 7413–7449. https://doi.org/10.1002/2015JC011047

Fu, L., Chelton, D., Le Traon, P., & Oceanography, M. R. (2010). Eddy dynamics from satellite altimetry. *Oceanography*, *23*(4), 14–25. https://doi.org/10.2307/24860859

Gill, A., Green, J., & Simmons, A. (1974). Energy partition in the large-scale ocean circulation and the production of mid-ocean eddies. *Deep-Sea Research and Oceanographic Abstracts*, *21*(7), 499–528. https://doi.org/10.1016/0011-7471(74)90010-2

Hogg, A. M., & Blundell, J. R. (2006). Interdecadal variability of the southern ocean. *Journal of Physical Oceanography*, *36*(8), 1626–1645. https://doi.org/10.1175/JPO2934.1

Hogg, A. M., Meredith, M. P., Chambers, D. P., Abrahamsen, E. P., Hughes, C. W., & Morrison, A. K. (2015). Recent trends in the Southern Ocean eddy field. *Journal of Geophysical Research: Oceans*, *120*(1), 257–267. https://doi.org/10.1002/2014JC010470

Hoyer, S., & Hamman, J. (2017). xarray: ND labeled arrays and datasets in Python. *Journal of Open Research Software*, *5*, 10. https://doi.org/10.5334/jors.148

Hu, S., Sprintall, J., Guan, C., McPhaden, M. J., Wang, F., Hu, D., & Cai, W. (2020). Deep-reaching acceleration of global mean ocean circulation over the past two decades. *Science Advances*, *6*(6), eaax7727. https://doi.org/10.1126/sciadv.aax7727

Japan Meteorological Agency, Japan. (2013). *JRA-55: Japanese 55-year reanalysis, daily 3-hourly and 6-hourly data*. Research Data Archive at the National Center for Atmospheric Research, Computational and Information Systems Laboratory. https://doi.org/10.5065/D6HH6H41

Kang, D., & Curchitser, E. N. (2013). Gulf Stream eddy characteristics in a high-resolution ocean model. *Journal of Geophysical Research: Oceans*, *118*(9), 4474–4487. https://doi.org/10.1002/jgrc.20318

Kang, D., & Curchitser, E. N. (2017). On the evaluation of seasonal variability of the ocean kinetic energy. *Geophysical Research Letters*, *47*(7), 1675–1583. https://doi.org/10.1175/JPO-D-17-0063.1

Li, G., Cheng, L., Zhu, J., Trenberth, K. E., Mann, M. E., & Abraham, J. P. (2020). Increasing ocean stratification over the past half-century. *Nature Climate Change*, *10*(12), 1116–1123. https://doi.org/10.1038/s41558-020-00918-2

Martínez-Moreno, J., Hogg, A. M., England, M., Constantinou, N. C., Kiss, A. E., & Morrison, A. K. (2021). Global changes in oceanic mesoscale currents over the satellite altimetry record. *Nature Climate Change*, *11*(5), 397–403. https://doi.org/10.1038/s41558-021-01006-9

Martínez-Moreno, J., Hogg, A. M., & England, M. H. (2022). Coherent and non-coherent Eddy Kinetic Energy and gridded coherent eddy statistics [Dataset]. Zenodo. https://doi.org/10.5281/zenodo.4646429

Martínez-Moreno, J., Hogg, A. M., Kiss, A. E., Constantinou, N. C., & Morrison, A. K. (2019). Kinetic energy of eddy-like features from sea surface altimetry. *Journal of Advances in Modeling Earth Systems*, *11*(10), 3090–3105. https://doi.org/10.1029/2019MS001769

Patel, R. S., Llort, J., Strutton, P. G., Phillips, H. E., Moreau, S., Pardo, P. C., & Lenton, A. (2020). The biogeochemical structure of Southern Ocean mesoscale eddies. *Journal of Geophysical Research: Oceans*, *125*(8), 1–24. https://doi.org/10.1029/2020jc016115

Pilo, G. S., Mata, M. M., & Azevedo, J. L. L. (2015). Eddy surface properties and propagation at Southern Hemisphere western boundary current systems. *Ocean Science*, *11*(4), 629–641. https://doi.org/10.5194/os-11-629-2015

Qiu, B. (1999). Seasonal eddy field modulation of the North Pacific Subtropical Countercurrent: TOPEX/Poseidon observations and theory. *Journal of Physical Oceanography*, *29*(10), 2471–2486. https://doi.org/10.1175/1520-0485(1999)029<2471:sefmot>2.0.co;2

Qiu, B., & Chen, S. (2004). Seasonal modulations in the eddy field of the South Pacific Ocean. *Journal of Physical Oceanography*, *34*(7), 1515–1527. https://doi.org/10.1175/1520-0485(2004)034<1515:smitef>2.0.co;2

Qiu, B., Chen, S., Klein, P., Sasaki, H., & Sasai, Y. (2014). Seasonal mesoscale and submesoscale eddy variability along the North Pacific Subtropical Countercurrent. *Journal of Physical Oceanography*, *44*(12), 3079–3098. https://doi.org/10.1175/JPO-D-14-0071.1

Rocklin, M. (2015). Dask: Parallel computation with blocked algorithms and task scheduling. *Proceedings of the 14th Python in Science Conference* (pp. 130–136). SciPy, 2015. https://doi.org/10.25080/Majora-7b98e3ed-013

Ruela, R., Sousa, M. C., de Castro, M., & Dias, J. M. (2020). Global and regional evolution of sea surface temperature under climate change. *Global and Planetary Change*, *190*, 103190. https://doi.org/10.1016/j.gloplacha.2020.103190

Samelson, R. M., Chelton, D. B., & Schlax, M. G. (2019). The ocean mesoscale regime of the reduced-gravity quasigeostrophic model. *Journal of Physical Oceanography*, *49*(10), 2469–2498. https://doi.org/10.1175/JPO-D-18-0260.1

Sasaki, H., Klein, P., Qiu, B., & Sasai, Y. (2014). Impact of oceanic-scale interactions on the seasonal modulation of ocean dynamics by the atmosphere. *Nature Communications*, *5*(1), 5636. https://doi.org/10.1038/ncomms6636

Schubert, R., Schwarzkopf, F. U., Baschek, B., & Biastoch, A. (2019). Submesoscale impacts on mesoscale Agulhas dynamics. *Journal of Advances in Modeling Earth Systems*, *11*(8), 2745–2767. https://doi.org/10.1029/2019ms001724

Siegel, D., Peterson, P., Dj, M., Maritorena, S., & Nelson, N. (2011). Bio-optical footprints created by mesoscale eddies in the Sargasso Sea. *Geophysical Research Letters*, *38*(13). https://doi.org/10.1029/2011GL047660

Stammer, D. (1998). On eddy characteristics, eddy transports, and mean flow properties. *Journal of Physical Oceanography*, *28*(4), 727–739. https://doi.org/10.1175/1520-0485(1998)028<0727:oeceta>2.0.co;2

Trasviña, A., Barton, E., Brown, J., Velez, H., Kosro, P. M., & Smith, R. L. (1995). Offshore wind forcing in the Gulf of Tehuantepec, Mexico: The asymmetric circulation. *Journal of Geophysical Research*, *100*(C10), 20649–20663. https://doi.org/10.1029/95jc01283

Uchida, T., Abernathey, R., & Smith, S. (2017). Seasonality of eddy kinetic energy in an eddy permitting global climate model. *Ocean Modelling*, *118*, 41–58. https://doi.org/10.1016/j.ocemod.2017.08.006

Wang, Q., & Tang, Y. (2022). The interannual variability of eddy kinetic energy in the Kuroshio large meander region and its relationship to the Kuroshio latitudinal position at 140°E. *Journal of Geophysical Research: Oceans*, *127*(2). https://doi.org/10.1029/2021jc017915

Willett, C. S., Leben, R. R., & Lavín, M. F. (2006). Eddies and tropical instability waves in the eastern tropical Pacific: A review. *Progress in Oceanography*, *69*(2–4), 218–238. https://doi.org/10.1016/j.pocean.2006.03.010

Wunsch, C. (2020). Is the ocean speeding up? Ocean surface energy trends. *Journal of Physical Oceanography*, *50*(11), 1–45. https://doi.org/10.1175/jpo-d-20-0082.1

Wunsch, C., & Ferrari, R. (2004). Vertical mixing, energy, and the general circulation of the oceans. *Annual Review of Fluid Mechanics*, *36*(1), 281–314. https://doi.org/10.1146/annurev.fluid.36.050802.122121

Wyrtki, K., Magaard, L., & Hager, J. (1976). Eddy energy in the oceans. *Journal of Geophysical Research*, *81*(15), 2641–2646. https://doi.org/10.1029/JC081i015p02641

Yue, S., & Wang, C. (2004). The Mann-Kendall test modified by effective sample size to detect trend in serially correlated hydrological series. *Water Resources Management*, *18*(3), 201–218. https://doi.org/10.1023/b:warm.0000043140.61082.60

Zamudio, L., Hurlburt, H. E., Metzger, E. J., Morey, S. L., O'Brien, J. J., Tilburg, C., & Zavala-Hidalgo, J. (2006). Interannual variability of Tehuantepec eddies. *Journal of Geophysical Research*, *111*(C5), 23. https://doi.org/10.1029/2005JC003182

Zheng, S., Feng, M., Du, Y., Meng, X., & Yu, W. (2018). Interannual variability of eddy kinetic energy in the subtropical southeast Indian Ocean associated with the El Niño-Southern Oscillation. *Journal of Geophysical Research: Oceans*, *123*(2), 1048–1061. https://doi.org/10.1002/2017jc013562